

Evaluation of cooling rate on electrochemical behavior of Sn–0.3Ag–0.9Zn solder alloy in 3.5 wt% NaCl solution

Huan Wang · Zhiming Gao · Yongchang Liu · Chong Li · Zongqing Ma · Liming Yu

Received: 9 August 2014 / Accepted: 3 October 2014 / Published online: 21 October 2014
© Springer Science+Business Media New York 2014

Abstract The corrosion resistance of Sn–0.3Ag–0.9Zn alloy solidified under different cooling rates in 3.5 wt% NaCl solution was evaluated based on potentiodynamic polarization, electrochemical impedance spectroscopy and electrochemical noise. It is found that the corrosion resistance of this alloy improves with the increase of the applied cooling rate, which is attributed to the distinct microstructure. The furnace-cooled and air-cooled alloy with active Zn-rich phase and a microstructure formed by a coarser dendritic array associated with larger size of AgZn₃ intermetallic compounds exhibit a worse corrosion resistance due to a serious galvanic corrosion. Besides, the Mott–Schottky measurement and the X-ray photoelectron spectroscopy were performed to analyze the semiconductor properties and composition of the passive film formed on the surface of the alloy. It confirms that the stability and protective ability of the passive films formed on furnace-cooled and air-cooled alloy are worse than that of water-cooled alloy due to their higher oxygen vacancy defects and concentration of unstable SnO. Furthermore, the major corrosion product on the surface of the Sn–0.3Ag–0.9Zn alloys is tin oxide chloride hydroxide.

1 Introduction

The traditional Sn–Pb eutectic solder alloy has been widely used in electronic industries in the last decades due to its

outstanding physical and mechanical properties. However, the toxicity of Pb to the human health and its danger to the environment has prompted many studies on the microstructure, metallurgical and mechanical properties of Pb-free candidate solder alloys.

Among these new lead-free solders, the eutectic Sn–9wt%Zn alloy appears to be an attractive alternative, with a low cost and a melting temperature of 198 °C which is relatively close to the traditional eutectic Sn–Pb solder. Its eutectic structure consists of two phases: a body centered tetragonal Sn matrix phase and a secondary phase of hexagonal Zn containing <1 % tin in solid solution [1]. For some electronic packaging methods and components, e.g. surface mounting technology (SMT), plating through hole (PTH) and ball grid array (BGA), the soldered interface can be directly exposed not only to the air, but also moisture and other corrosion media, such as brackish coastal atmosphere [1, 2]. However, Zn is easily oxidized and it is susceptible to corrosion, which limited the application of the Sn–Zn alloy. Takemoto and Funaki [3] have established that the addition of Ag to the Sn–9Zn solder alloy inhibits the anodic dissolution of Zn and enhances the wettability of solder alloy on a Cu substrate [4–6]. Besides, Lee et al. [5] confirmed that the incorporation of Ag into Sn–Zn eutectic alloy is effective for improvement of the oxidation resistance, whereas alloys with lower Ag content have been found as better corrosion resistance material since the high volume fraction of Ag₃Sn will accelerate the galvanic corrosion [7]. Thus, we selected Sn–0.3Ag–0.9Zn (a low Ag and low Zn) alloy as the subject of this research to examine its electrochemical behavior in 3.5 wt% NaCl solution to simulate seawater and address the possible corrosion problem that may occur in the marine environment, which was scarcely studied before.

On the other hand, the cooling rate during soldering led to distinct microstructural arrays which usually

H. Wang · Z. Gao (✉) · Y. Liu (✉) · C. Li · Z. Ma · L. Yu
State Key Lab of Hydraulic Engineering Simulation and Safety,
School of Materials Science and Engineering, Tianjin
University, Tianjin 300072, People's Republic of China
e-mail: gaozhiming@tju.edu.cn

Y. Liu
e-mail: licmtju@163.com

affect the corresponding corrosion behavior of the solder alloys [8–13]. The rapidly solidified Sn–3.0Ag–0.5Cu (SAC305) solder with smallest Ag₃Sn intermetallic compounds (IMCs) exhibits better corrosion resistance than air-cooled and furnace-cooled SAC305 solders because microgalvanic corrosion between large cathodic Ag₃Sn IMCs plates and anodic Sn matrix decreases the corrosion resistance of air-cooled and furnace-cooled SAC305 solders [13]. Osório et al. [14] evaluated the morphology of intermetallic particles, the segregation pattern and the resulting corrosion potential, corrosion rate and polarization resistance of Sn–2.8wt%Cu solder alloy solidified in different cooling rates, which showed that the cooling rate plays an important role on the microstructure formation affecting significantly the corresponding electrochemical behavior.

Therefore, the present study aims to investigate the effect of cooling rate on the electrochemical behavior of Sn–0.3Ag–0.9Zn alloy in 3.5 wt% NaCl solution. The solidification processes under different cooling rates were systematically explored by optical microscope (OM), scanning electron microscope (SEM) equipped with the energy dispersive X-ray (EDX) detector and differential scanning calorimetry (DSC). Furthermore, the electrochemical behavior of samples was inspected through the potentiodynamic polarization tests, electrochemical impedance spectroscopy (EIS) and electrochemical noise (EN). Meanwhile, it is believed that the corrosion resistance of metal is also strongly related to the properties of the passive film formed on the surface in such environment [15–17]. Thus, Mott–Schottky plots and X-ray photoelectron spectroscopy (XPS) were applied to characterize the semiconductor structure properties and the composition of the passive film formed on the surface of the samples in NaCl solution.

2 Experimental procedure

2.1 Specimens preparation

The Sn–0.3Ag–0.9Zn solders (in mass) were prepared from bulk Sn, Ag and Zn rods (all with a purity of 4 N). The process of melting was carried out in a vacuum arc furnace under the protection of high purity argon atmosphere to produce button-like specimen with a diameter of approximate 35 mm. Considering the high volatility of zinc, the zinc and silver particles were put at the bottom covered with tin blocks. So, with the melting current controlled carefully all the time, tin first melted and then its liquid surrounded the zinc and silver particles during the melting to avoid zinc's evaporating. In order to get a homogeneous composition, the ingot was remelted for four times.

Table 1 The achieved cooling rates by cooling in different media

Cooling condition	Cooling rate (K s ⁻¹)
Furnace-cooled	0.08
Air-cooled	6.5
Water-cooled	100

Then, cut the specimen into three parts. The three parts were remelted and solidified to the ambient temperature under three different cooling rates obtained by changing the cooling media: furnace, air and water. Table 1 lists the applied cooling rates of the three samples.

2.2 Microstructure observation

In order to observe microstructure, the specimens were mounted in an epoxy resin, then grounded by using SiC papers up to 2,000 grit, polished with 0.05 mm alumina powders, and etched by an etchant of 4 vol% HNO₃ + 96 vol% C₂H₅OH. An Olympus C-35A OM and a Phillips-XL30 SEM equipped with an EDX detector were used for observation of microstructures and determination of the phase composition respectively. Besides, a Mettler Toledo DSC was employed to determine the melting and solidification behavior.

2.3 Electrochemical measurement

The Sn–0.3Ag–0.9Zn alloy specimens were cut into 10 mm × 10 mm × 3 mm, and then embedded in epoxy resin leaving an area of 1 cm² exposed to the solution. The working surfaces were wet grounded with SiC metallurgical waterproof abrasive papers up to 2,000 mesh, followed by ultrasonic cleaning in alcohol and finally rinsed in deionized water. The test solution was prepared with deionized water and reagent-grade NaCl (3.5 wt%) to simulate a seawater environment.

All electrochemical measurements except EN were performed using an Autolab 302 N electrochemical workstation at ambient temperature (25 ± 2 °C) in a conventional three-electrode cell, a 10 mm × 10 mm × 0.2 mm platinum plate as the counter electrode (CE) and a saturated calomel electrode (SCE) as the reference electrode (RE). For each experimental condition, at least three measurements were conducted on separate specimens to assert the reliability of the result.

2.3.1 Potentiodynamic polarization

Prior to the potentiodynamic polarization measurement, the specimens were kept in solutions for about 10 min until a

stable open circuit potential (OCP) was reached. Potentiodynamic polarization was applied by sweeping the potential in the positive direction at 10 mV/min (~0.1667 mV/s) from -50 mV (vs. OCP) until the current density reached 1 mA/cm².

2.3.2 EIS measurements

EIS measurements, which are widely accepted as a powerful and non-destructive tool, were performed at the free corrosion potential after different immersing times in the investigated solution with a 10 mV amplitude signal and a range of applied frequency from 10 kHz to 100 mHz with the frequency values spaced logarithmically (eight per decade).

2.3.3 EN measurements

Although EN is scarcely applied to investigate the solder alloys, it is able to instantaneously monitor the rate of the corrosion process and carry out without artificial disturbance of the system compared to the common electrochemical techniques. Thus, in this research, EN was measured by a CST500 electrochemical noise meter (Corrtest Instrument, China), in which an auto zero resistance ammeter (ZRA) and a high impedance voltage follower (HVF) were embedded. The ZRA was employed to measure the coupling current between the above two nominally identical working electrodes (WEs). At the same time, with a SCE as RE, the HVF was employed to measure the voltage noise of the coupled WEs against RE. EN data was simultaneously recorded with time for 6 h. Each set of EN records, containing 1,024 data points, recorded with a data-sampling interval of 0.2 s. 105 time records were analyzed. The data was trend removed using 5th polynomial fitting. The noise resistance R_n [18] was calculated as:

$$R_n = \frac{\sigma_E}{\sigma_I} \tag{1}$$

where σ_E is the standard deviation of potential noise and σ_I is the standard deviation of the current noise. R_n is inversely proportional to the corrosion rate when both working electrodes have the same activity and the corrosion process is uniform and activation controlled [19].

2.3.4 Mott–Schottky measurements

Mott–Schottky analysis was performed to identify the semiconductor properties of the oxide film on Sn–0.3Ag–0.9Zn solder surfaces. The potential scan direction was from the anodic to cathodic, with a scanning interval of 50 mV. An alternating current (AC) signal with a frequency of 1,000 Hz and a peak-to-peak magnitude of

10 mV was superimposed on the scanning potential and the capacitance was measured at each applied potential.

Since the space charge region developed in the oxide film and the Helmholtz layer can be considered as two capacitors in series, the capacitance of the film–electrolyte interface in Mott–Schottky form is as follow [20]:

$$\frac{1}{C^2} = \frac{1}{C_{SC}^2} + \frac{1}{C_H^2} + \frac{2}{C_{SC}C_H} \tag{2}$$

where C_{SC} and C_H are the space charge and the Helmholtz capacitance, respectively. The doping densities of classical semiconductors are usually in the order of 10¹⁶ cm⁻³. In this case, $C_{SC} \ll C_H$, therefore, the second and third terms can be neglected and the measured capacitance C is equal to the space charge capacitance C_{SC} . According to the Mott–Schottky theory, the space charge capacitance (C_{SC}) of n-type and p-type semiconductor are given by Eqs. 3 and 4, respectively [20, 21];

$$\frac{1}{C^2} = 2(E - E_{fb} - kT/e)/(\epsilon\epsilon_0eN_D A^2) \tag{3}$$

for n-type semiconductor

$$\frac{1}{C^2} = -2(E - E_{fb} - kT/e)/(\epsilon\epsilon_0eN_A A^2) \tag{4}$$

for p-type semiconductor

where e is the elementary charge of electrons ($e = -1.602 \times 10^{-19}$ C), A is the geometrical surface area, N_D and N_A are the donor density for n-type semiconductor and acceptor density for p-type semiconductor, respectively, in the passive film, E_{fb} is the flat-band potential, E is the applied potential under depletion conditions, ϵ is the dielectric constant of the oxide film, which is assumed as 12, ϵ_0 is the vacuum permittivity (8.854×10^{-14} F/cm), k is the Boltzmann constant (1.38×10^{-23} J/K), T is the absolute temperature. From Eqs. 3 and 4, N_D and N_A can be derived from the slope of the experimental C^{-2} versus E plots.

2.4 Surface analysis

The passive films formed by polarizing at the potential of passivation (-0.55 V_{SCE}) for 1 h were studied by a commercial X-ray photoelectron spectroscopy (PHL1600ESCA XPS). And the calculations of the data were performed using XPS Peak 4.1 peak-fitting software. Besides, the morphology and compositions of surface corrosion products were investigated using SEM and EDX.

3 Results and discussion

3.1 Thermal properties and microstructures

Figure 1 illustrates the measured DSC curves of the investigated Sn–0.3Ag–0.9Zn alloy at a heating and

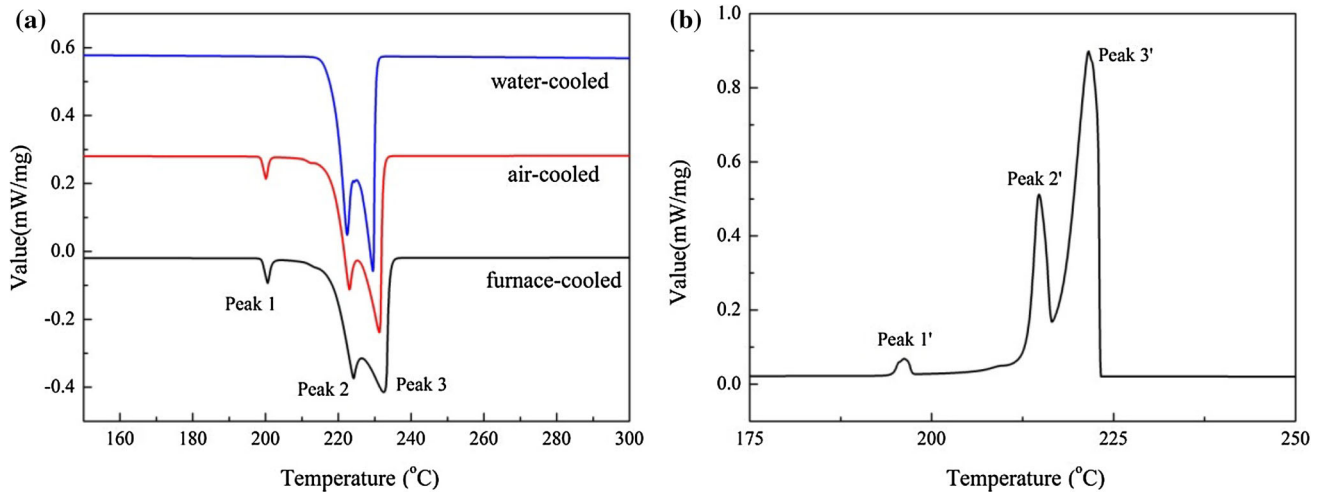


Fig. 1 **a** DSC curves of the Sn–0.3Ag–0.9Zn alloy solidified under different cooling rates upon heating (heating rate: 5 K/min); **b** DSC curve of water-cooled Sn–0.3Ag–0.9Zn alloy upon cooling (cooling rate: 5 K/min)

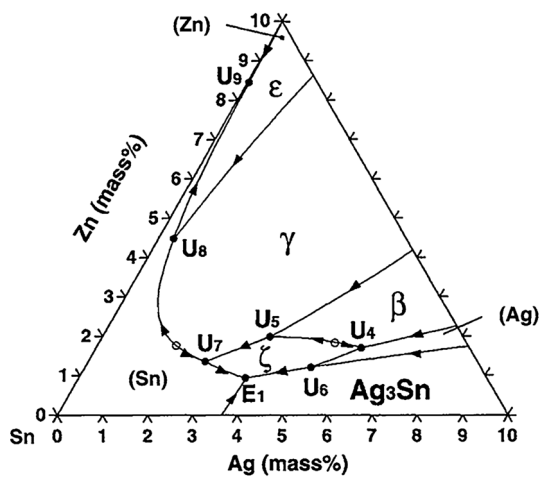


Fig. 2 Sn-rich portion of the liquidus surface of the Sn–Ag–Zn system [23]

cooling rate of 5 K/min, which reveals their melting and solidification behavior. According to the Sn–Ag–Zn ternary phase diagram (see Fig. 2), the reactions for each peak in the thermal analysis curve upon heating are presented in Table 2, which was also investigated by previous researches [22, 23]. Moreover, it is found that the temperature for each peak shifts to the high temperature direction as each reaction needs some superheating. Besides, upon heating, there are two melting peaks occurring in the water-cooled alloy and three peaks taking place in furnace-cooled and air-cooled alloys. However, peak 1' occurs in the DSC curve of water-cooled Sn–0.3Ag–0.9Zn alloy upon cooling (see Fig. 1b). It confirms that the rapid cooling rate inhibits the occurrence of the reaction ($L + \varepsilon\text{-AgZn}_3 \rightarrow \beta\text{-Sn} + \text{Zn}$) which generates the Zn-rich phase.

Table 2 The corresponding reactions occurring in the DSC curve of the Sn–0.3Ag–0.9Zn (see Fig. 1)

Peak	Temperature (°C)	Reaction
1	193.7	Peritectic reaction: $\beta\text{-Sn} + \text{Zn} \rightarrow L + \varepsilon\text{-AgZn}_3$ [U_9] [23]
2	209.7	Peritectic reaction: $\beta\text{-Sn} + \varepsilon\text{-AgZn}_3 \rightarrow L + \gamma\text{-Ag}_5\text{Zn}_8$ [U_8] [23]
3		Melting reaction: $S \rightarrow L$

The OM images and the SEM images of the Sn–0.3Ag–0.9Zn alloys solidified under different cooling rates are shown in Fig. 3, depicting the $\beta\text{-Sn}$ (dendritic matrix) and a mixture of IMCs locating in the interdendritic regions. From the Fig. 3, it can be clearly seen that the size of both the primary $\beta\text{-Sn}$ and IMCs decreases with the increase of the cooling rate. Besides, the chemical composition of each phase is determined by EDX analysis, and the obtained EDX results of the typical IMCs in furnace-cooled Sn–0.3Ag–0.9Zn alloy (see Fig. 3b) are shown in Table 3. The atomic ration of EDX 1 is about 1Ag:3Zn, which is $\varepsilon\text{-AgZn}_3$ IMCs particle. Furthermore, due to the trace amount of Zn, though EDX 2 detected a large number of matrix element Sn, the needle-like IMCs are Zn-rich phases, which was also found in Sn–9Zn and Sn–9Zn–0.5Ag–1In alloy [24, 25]. Overall, considering the DSC analyses, Sn–Ag–Zn ternary phase diagram and the EDX results, the IMCs in interdendritic region of furnace-cooled and air-cooled alloys are relatively coarser granular AgZn_3 phase and needle-like Zn-rich phase, while only fine AgZn_3 IMCs particles exist in the interdendritic region of the water-cooled alloy.

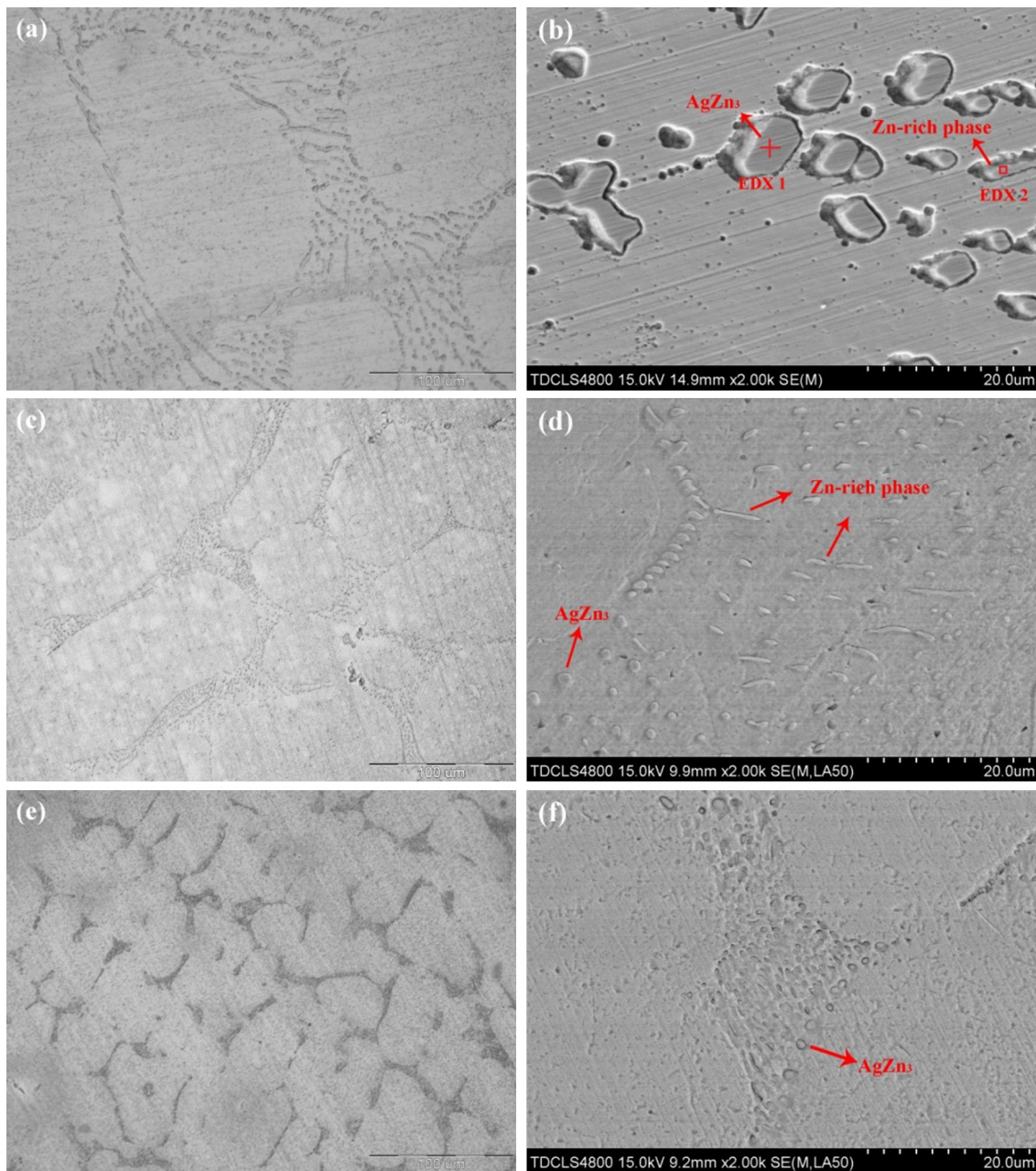


Fig. 3 OM images and SEM images of the Sn–0.3Ag–0.9Zn alloy solidified under different cooling rates, **a, b** furnace-cooled, **c, d** air-cooled and **e, f** water-cooled

According to the investigation of Chang et al. [24], the appearance of the Zn-rich phase is the crucial reason for the inferior corrosion resistance of the Sn–9Zn–0.5Ag–1In solder alloy. Furthermore, the IMCs with a large size also deteriorate the corrosion resistance of alloy due to the microgalvanic corrosion between the cathodic IMCs and the anodic Sn matrix [13]. Therefore, the furnace-cooled and air-cooled alloy with Zn-rich phase and coarse IMCs are speculated to have a worse corrosion resistance.

3.2 Potentiodynamic polarization

A comparison of experimental potentiodynamic polarization curves of the Sn–0.3Ag–0.9Zn alloy samples in 3.5 % NaCl solution at ambient temperature are shown in Fig. 4. The Sn–0.3Ag–0.9Zn alloy exhibits self-passivation characteristics in three cooling rates, with a wide passive potential range, which suggests that there is a protective oxide film spontaneously forming on the surface of the Sn–0.3Ag–0.9Zn alloy when it is immersed in the test solution.

The electrochemical properties of Sn–0.3Ag–0.9Zn solidified under different cooling rates in 3.5 % NaCl solution obtained from Fig. 4 are listed in Table 4.

The corrosion potentials (E_{corr}) are -0.943 , -0.875 and -0.812 V_{SCE} for furnace-cooled, air-cooled and water-cooled alloys, respectively. It indicates that the value of E_{corr} shifts towards noble value with the increase of the cooling rate. Besides, it is found that the E_{corr} of Sn–0.3Ag–0.9Zn alloy in 3.5 % NaCl solution is more positive than that of other Sn–Zn alloys, such as the -1.43 V_{SCE} of Sn–9Zn, -1.07 V_{SCE} of Sn–9Zn–0.5Ag, -1.09 V_{SCE} of Sn–9Zn–0.5Ag–1In [6] and (-1.160 to -1.207 V_{SCE}) of Sn–8.5Zn–xAg–0.1Al–0.05 Ga ($x = 0.1$ – 2 wt%) [16]. Furthermore, the corrosion current densities (i_{corr}) were estimated from the Tafel plots using both cathodic and anodic branches of the polarization curves from $-50/70$ mV (vs. OCP). As depicted in Fig. 4 and listed in Table 4, the value of i_{corr} and the average passive current density (i_{pa}) in the whole passive range decreases obviously with increasing cooling rate. Moreover, the passive film appears to break down at a certain potential. As for the furnace-cooled and air-cooled alloys, their pitting potentials (E_p) are about 20 mV lower than that of the water-cooled alloy. In general, the increase in cooling rate in the Sn–0.3Ag–0.9Zn alloy results in the improvement of the corrosion resistance and the protection from the oxide film formed on the surface of the alloy, which is consistent with the speculation based on the microstructure of the alloy.

3.3 EIS and EN

Figure 5a, b shows the effect of cooling rate on the impedance spectra (Nyquist plot and Bode plot) for the Sn–0.3Ag–0.9Zn alloy after being immersed in the solution for 2 h and 6 h. In the impedance measurement, the radius of

the semi-circular arc (see Fig. 5a) enlarges with prolonging immersion time from 2 to 6 h, showing typical features that are often observed for a passive film forming on the alloy [19] and an enhancement of its protective behavior [26]. Besides, the radius of the capacitive loop observed in Fig. 5a and the module in low frequency (0.1 Hz) observed in Fig. 5b are consistent with the potentiodynamic results presented in Fig. 4 where a minimum i_{pa} ($2.5 \mu\text{A}/\text{cm}^2$) occurs in the water-cooled alloy and a maximum one ($17 \mu\text{A}/\text{cm}^2$) in the furnace-cooled alloy.

This trend is also verified by the EN results. Figure 6 shows the potential noise and current noise as a function of time during immersion in the 3.5 % NaCl solution for 6 h. The potential noise presents a trend of gradual growth, while the current noise reduces progressively until a certain value reaches. The initial decrease of current density corresponds to the formation of passive film on the electrode surfaces [27]. Compared the alloys solidified in different medium, the water-cooled alloy has the most positive potential and the minimum current fluctuation, which are consistent with the potentiodynamic results presented in Fig. 4 and the EIS results shown in Fig. 5. Furthermore, the calculated noise resistance (R_n) as a function of immersing

Table 3 EDX results of the indicated structure in Fig. 3b

Elements	Position (at.%)	
	EDX 1	EDX2
Zn	70.5	19.0
Ag	29.5	
Sn		81.0

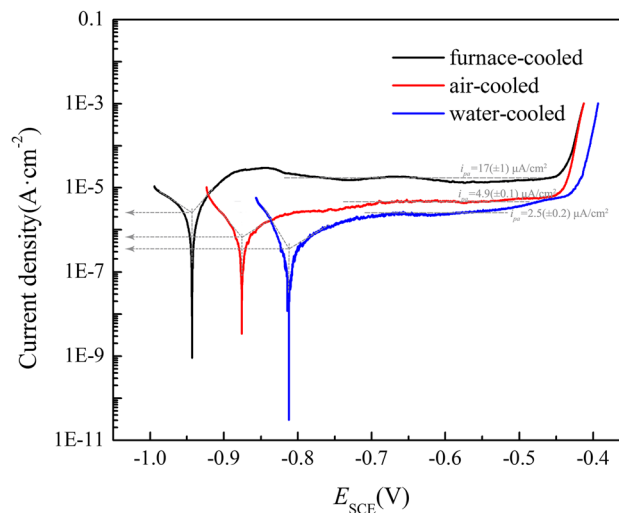


Fig. 4 Potentiodynamic polarization curves obtained for Sn–0.3Ag–0.9Zn in 3.5 % NaCl solution at a scan rate of 0.1667 mV/s at room temperature

Table 4 Electrochemical properties of Sn–0.3Ag–0.9Zn solidified under different cooling rates in 3.5 % NaCl solution

	E_{corr} (V/SCE)	i_{corr} ($\mu\text{A}/\text{cm}^2$)	i_{pa} ($\mu\text{A}/\text{cm}^2$)	E_p (V/SCE)
Furnace-cooled	$-0.943 (\pm 0.002)$	$2.8 (\pm 0.2)$	$17 (\pm 1)$	$-0.449 (\pm 0.001)$
Air-cooled	$-0.875 (\pm 0.004)$	$0.67 (\pm 0.03)$	$4.9 (\pm 0.1)$	$-0.450 (\pm 0.001)$
Water-cooled	$-0.812 (\pm 0.002)$	$0.35 (\pm 0.02)$	$2.5 (\pm 0.2)$	$-0.431 (\pm 0.002)$

E_{corr} , corrosion potential; i_{corr} , corrosion current density; i_{pa} , passive current density; E_p , pitting potential

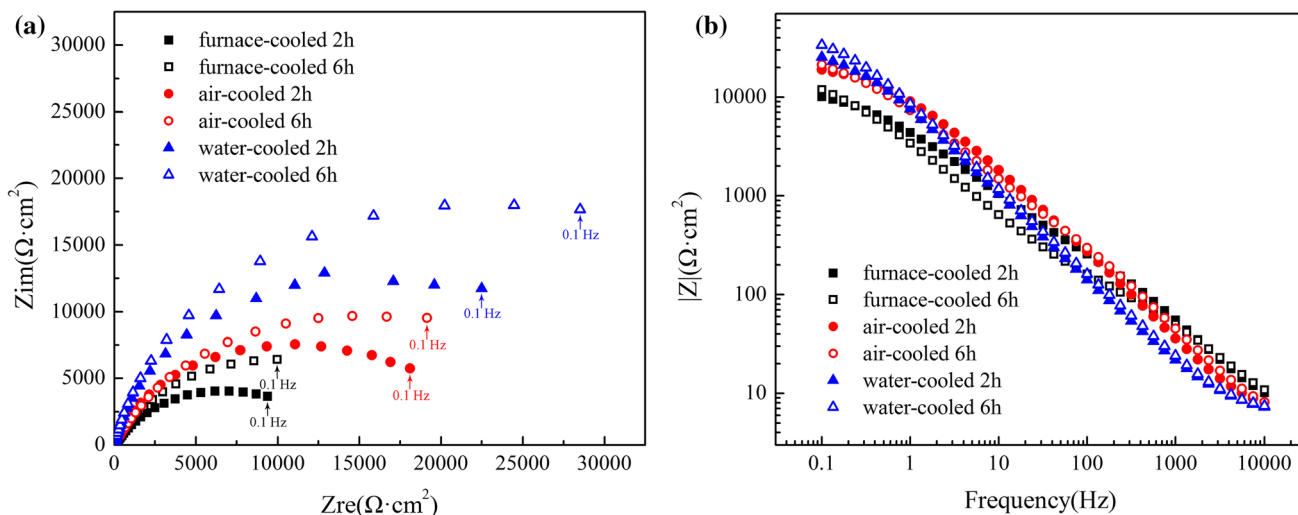


Fig. 5 EIS plots of Sn–0.3Ag–0.9Zn alloy solidified under different cooling rates after immersed in 3.5 % NaCl solution for 2 h and 6 h: **a** Nyquist plot. **b** Bode plot

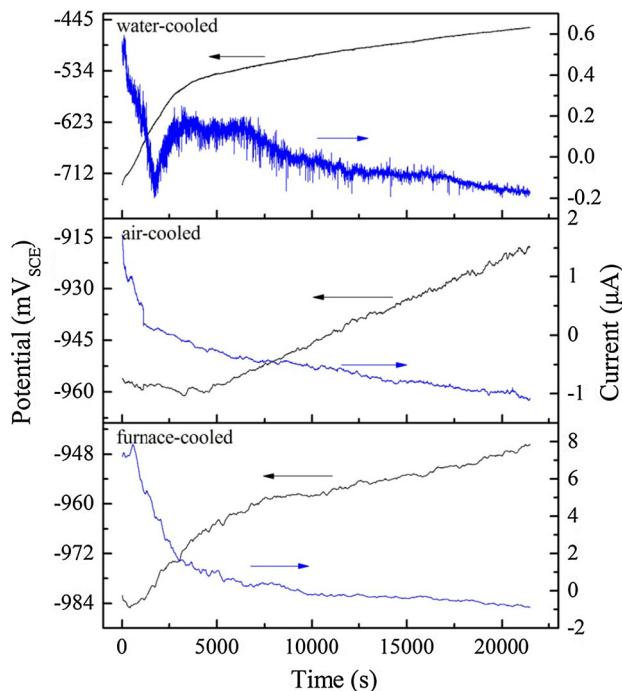


Fig. 6 EN plots of Sn–0.3Ag–0.9Zn alloy solidified under different cooling rates during an immersion of 6 h

time obtained from EN data is plotted in Fig. 7. The noise resistance (R_n) enhances continuously and slightly as time goes on, implying the growth process of the passive film. On the whole, it is observed that the R_n value of alloys in 3.5 % NaCl solution decreases in the following order: the water-cooled alloy (approximately 80 K Ω) > the air-cooled alloy (approximately 11 K Ω) > the furnace-cooled alloy (approximately 8 K Ω). Since R_n is inversely proportional to the corrosion rate, the differences between R_n

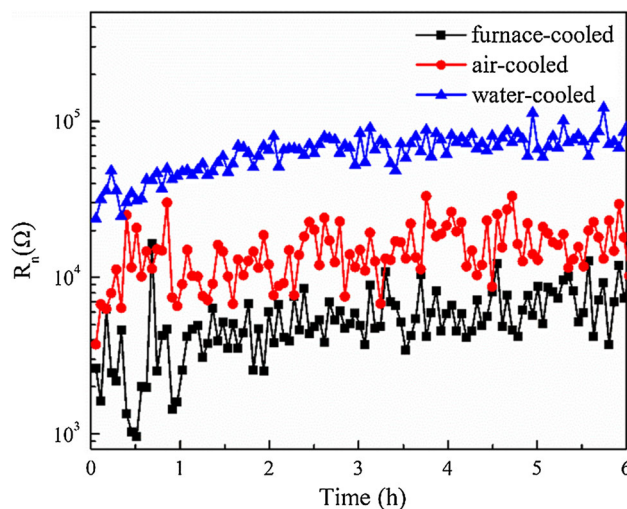


Fig. 7 Calculated noise resistances (R_n) as a function of immersing time obtained from EN data

values indicate the different dissolution rates of the passive films.

3.4 Semiconductor properties of the passive film

Specifically, the alloys show self-passivation properties by forming a passive film at the surface in test solution, which was observed through the electrochemical measurements. Moreover, this passive film on the surface has semiconductor properties, and we can get precise information in terms of the concentration of flaws (cation vacancy and oxygen vacancy) of the passive film by studying on their semiconductor structure properties, which determine the stability and protective ability of the passive film.

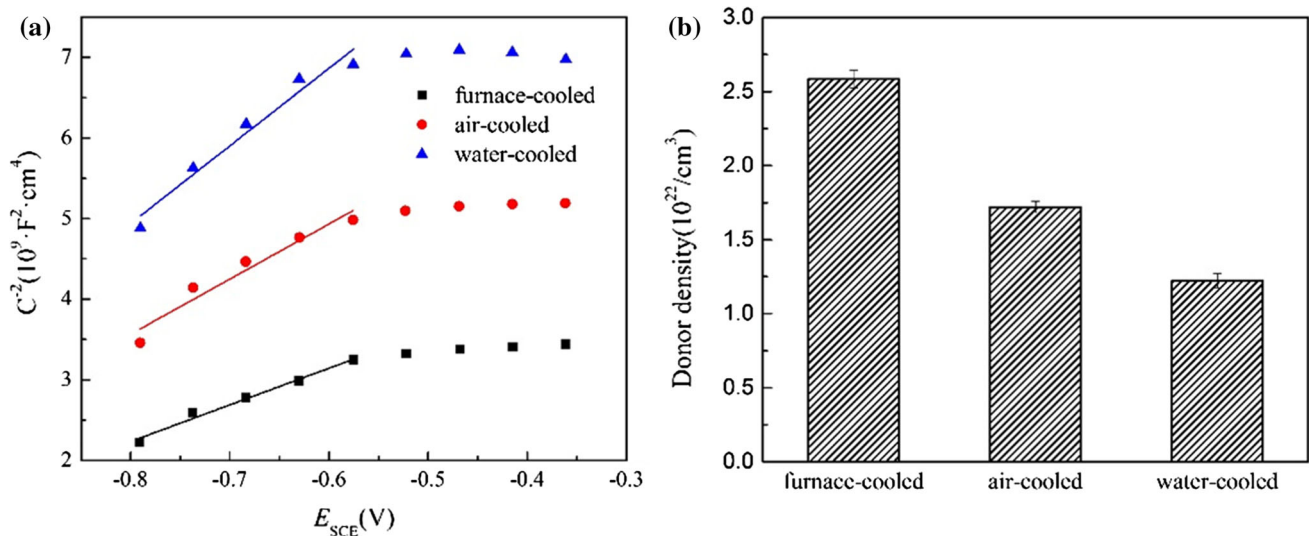


Fig. 8 **a** Mott–Schottky results of Sn–0.3Ag–0.9Zn alloy solidified under different cooling rates; **b** the calculated donor density as a function of solution

Therefore, Mott–Schottky analyses were performed for Sn–0.3Ag–0.9Zn alloys solidified in different medium after passivation at about $-0.55 V_{\text{SCE}}$ for 1 h at ambient temperature. The potential was selected to be close to the pitting potential ($-0.45 V_{\text{SCE}}$) to help to understand the degradation mechanism.

Figure 8a shows that the passive films exhibit Mott–Schottky behavior when the film formation potentials are between -0.8 and $-0.58 V_{\text{SCE}}$. The Mott–Schottky curves of the samples under three cooling rates exhibit linear properties with the positive slopes in 3.5 % NaCl solution, which shows that the passive films all present n-type semiconductor behavior. It can be attributed to the presence of oxygen vacancies in the passive film.

According to the point defect model (PDM) [28], it is assumed that cation vacancies migrate from the oxide–electrolyte interface to the metal–oxide interface, which is equivalent to the transport of cations in the opposite direction. If these vacancies penetrate into the metal phase at a slower rate than their transport through the oxide, they accumulate at the metal–oxide interface and finally lead to a local concentration. The inward diffusion or migration of cation vacancies is affected by the incorporation of chloride at the oxide–electrolyte interface according to the following mechanism by which chloride ions can fill anion vacancies:



where $V_{\text{O}}^{\cdot\cdot}$ represents the oxygen vacancy at the film/solution interface and Cl_{O} represents a chloride ion occupying an oxygen vacancy at the same location. The system responds to the loss of oxygen vacancies by generating cation vacancy/oxygen vacancy pairs via a Schottky-pair formation type of reaction:



where $V_{\text{M}^{x+}}$ represents a cation vacancy. The newly generated oxygen vacancies can in turn react with additional chloride ions at the film/solution interface, generating more oxygen vacancies and cation vacancies. These processes (adsorption of chloride ions and generation of cation vacancies) are autocatalytic. As a result, redundant cation vacancies gradually accumulate on the metal/film interface, which isolate the metal substrate and the passive film, preventing the continual growth of the passive film. Eventually, the voids formed on the metal/film interface generate stress within the passive film, leading to the nucleation and propagation of pitting and final breakdown. Therefore, passive film containing more oxygen vacancies is more vulnerable to damage.

Besides, the concentration of the oxygen vacancy defect, quantified by N_{D} value in this situation, can be calculated from the slope of the linear potential region. The dependence of the donor concentrations (N_{D}) on the cooling rates of alloys is displayed in Fig. 8b. The N_{D} value diminishes from about $2.68 \times 10^{22} \text{ cm}^{-3}$ to about $1.25 \times 10^{22} \text{ cm}^{-3}$, indicating that the oxygen vacancies in the passive film decreased with the increase of cooling rates.

As a result, the stability and protective ability of the passive film formed on water-cooled alloy is higher than that of furnace-cooled alloy and air-cooled alloy, which is consistent with the polarization curves, EIS and EN.

3.5 Composition of the passive film

The passive films of the Sn–0.3Ag–0.9Zn alloys solidified under different medium were obtained by anodic

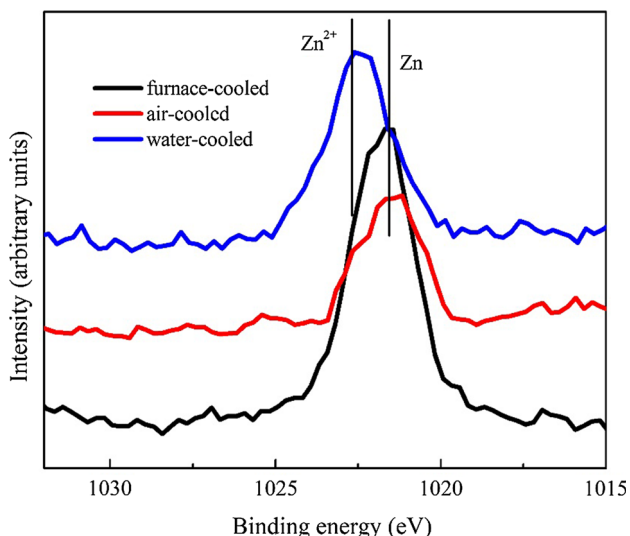
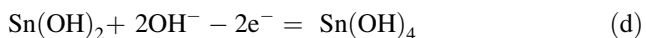
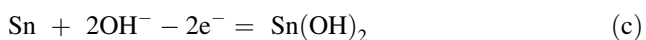


Fig. 9 XPS spectrum for Zn_{2p_{3/2}} obtained from Sn–0.3Ag–0.9Zn alloy solidified under different cooling rates polarized at $-0.55 V_{SCE}$ for 1 h in 3.5 % NaCl solution at room temperature: **a** furnace-cooled, **b** air-cooled, **c** water-cooled

polarization at $-0.55 V_{SCE}$ situated at passive region for 1 h and a steady-state current was attained in 3.5 % NaCl solution at room temperature. Then XPS was performed on the passive film and the results are shown in Fig. 9 (Zn_{2p_{3/2}} spectra) and Fig. 10 (Sn_{3d_{5/2}} spectra). From Fig. 9, the element of Zn existing as Zn²⁺ on the surface of the passive film forms on water-cooled alloy, while Zn⁰ on the surfaces of furnace-cooled and air-cooled alloy due to the presence of Zn-rich phases. As the weak points more susceptible to corrosion, the Zn⁰ on the surface of furnace-cooled and air-cooled alloys would accelerate the breakdown of the passive film.

In addition, the peak in Sn_{3d_{5/2}} spectra (see Fig. 10) is separated to three ones corresponding to binding energies of 484.2, 485.6 and 486.3 eV, which are signed to Sn, SnO and SnO₂ respectively [29]. As shown in Fig. 10, the oxide films on the surfaces of the Sn–0.3Ag–0.9Zn alloys solidified under different medium after anodic polarization at $-0.55 V_{SCE}$ for 1 h have the same composition, all containing SnO and SnO₂. According to the study of Alvarez et al. [30], in near neutral media, SnO and SnO₂ might form through the following steps:



The dehydration of Sn(OH)₂ into SnO and Sn(OH)₄ into SnO₂ was also reported as follows:



However, each composition in each cooling rate has different content. The ratio of SnO₂/(SnO + SnO₂) and SnO/(SnO + SnO₂) in the oxide films formed on the surface of samples under different cooling rates obtained from Fig. 10 is shown in Fig. 11. It is found that with the cooling rates increasing, the proportion of SnO₂ increases evidently. Besides, the Gibbs free energy of formation is -251.9 kJ/mol for SnO and -515.8 kJ/mol for SnO₂, implying that SnO₂ is expected to be more stable than SnO [31]. As a result, the stability and protective ability of the passive film formed on water-cooled alloy is higher than that of the other, which is consistent with the Mott–Schottky and other electrochemical measurements results.

3.6 Corrosion products analysis

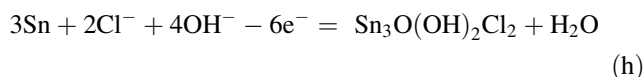
All solders were anodic polarized at $-0.3 V_{SCE}$ (higher than the pitting potential) for 120 s in 3.5 % NaCl solution at room temperature to obtain the corrosion products and contrast the corrosion situations. Figure 12 illustrates the surfaces of Sn–0.3Ag–0.9Zn alloys solidified under different cooling rates after the anodic polarization. The results show that all of the solders exhibit local corrosion behavior, especially for the furnace-cooled alloy (see Fig. 12a), of which the surface is the coarsest. In contrast, the water-cooled alloy has some smooth and uncorroded parts, shown in Fig. 12d. This result also confirms the corrosion resistance of water-cooled alloy is better than the furnace-cooled and air-cooled alloys, which is accorded with the consequence of electrochemical tests.

Besides, Fig. 12b reveals a mixture of compact, sheet-like corrosion products with pores and openings caused by the presence of Cl⁻ on the outer surface of the Sn–0.3Ag–0.9Zn solder, as well as the Sn–1Ag–0.5Cu–0.5Ni alloy polarized to 100 mV [32]. Based on the EDX analysis performed on the SEM micrograph in Fig. 12b, the corrosion products contain mainly Sn, Cl and O, at 35.92, 25.48 and 38.60 at.%, respectively.

During the polarization test in NaCl solution, the possible cathodic reaction is the dissolved oxygen reduction reaction [26]:



The reactions on the anode are quite complicated. After the breakdown of the passive film, under the damaging effect of the chlorine ions, some possible anodic reactions have been reported in the literatures [26, 33]:



Lots of researchers have studied the corrosion properties of Sn–Ag, Sn–Ag–Cu, Sn–Cu, Sn–Zn, Sn–Zn–Bi and

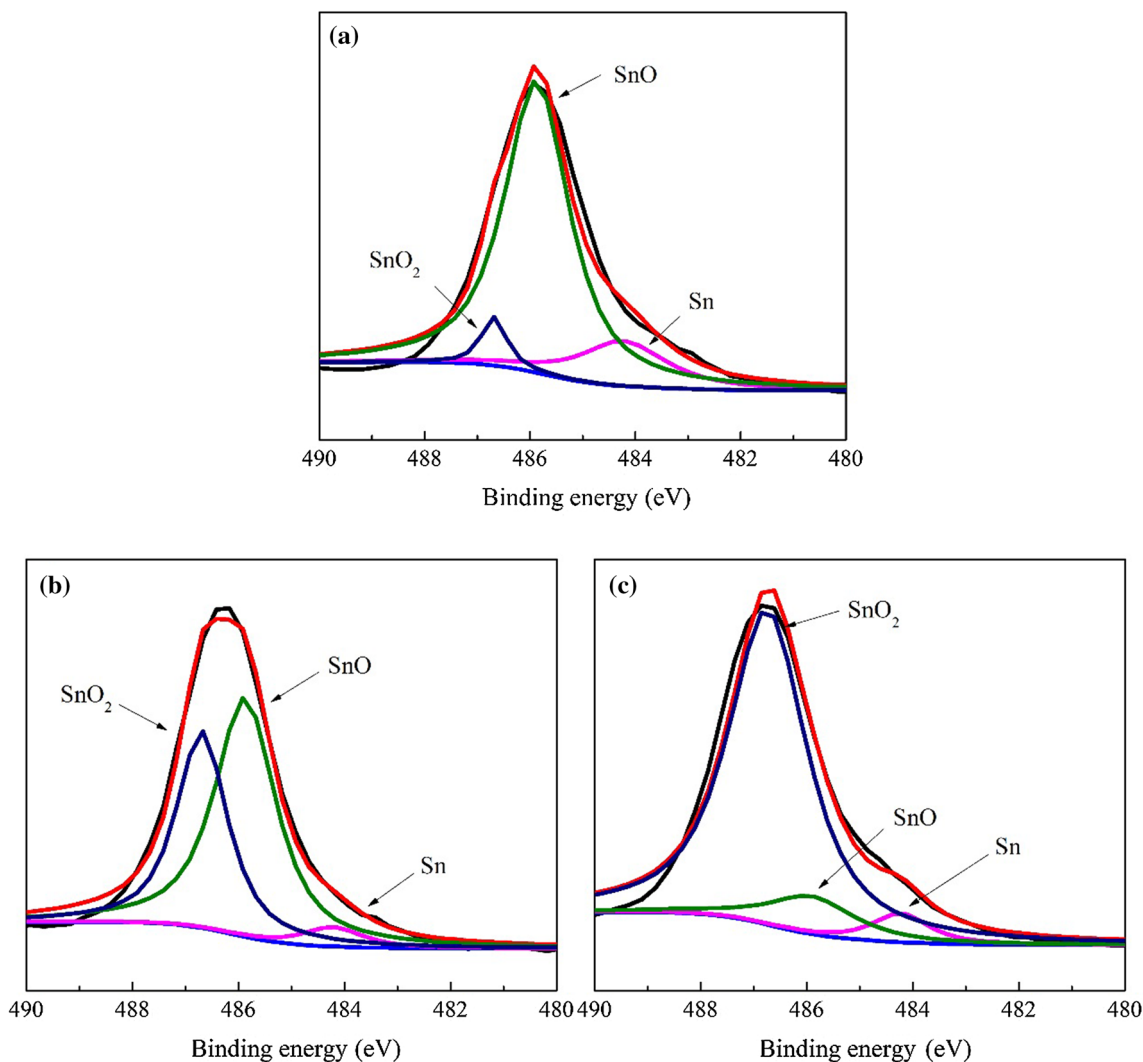


Fig. 10 XPS spectrum for $\text{Sn}3d_{5/2}$ obtained from $\text{Sn}-0.3\text{Ag}-0.9\text{Zn}$ alloy solidified under different cooling rates polarized at $-0.55 \text{ V}_{\text{SCE}}$ for 1 h in 3.5 % NaCl solution at room temperature: **a** furnace-cooled, **b** air-cooled, **c** water-cooled

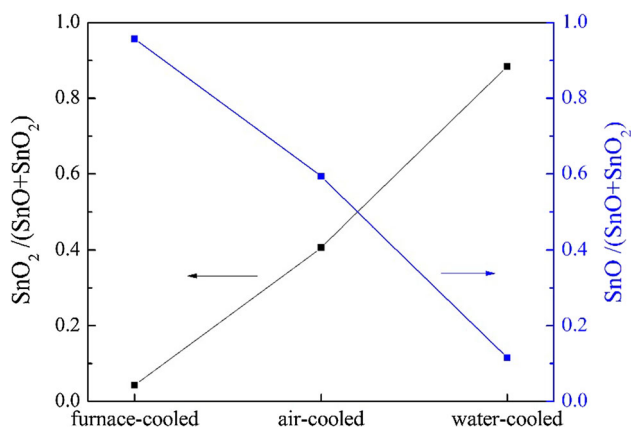


Fig. 11 The ratio of $\text{SnO}_2/(\text{SnO} + \text{SnO}_2)$ and $\text{SnO}/(\text{SnO} + \text{SnO}_2)$ in the oxide film formed on the surface of $\text{Sn}-0.3\text{Ag}-0.9\text{Zn}$ alloy obtained from Fig. 10

$\text{Sn}-\text{Pb}$ solders in 3.5 % NaCl solution, and their results showed that the corrosion product on the surface was needle-like tin oxyhydroxy chloride ($\text{Sn}_3\text{O}(\text{OH})_2\text{Cl}_2$) [2, 31–33]. Hence, from the studies above, the corrosion product of $\text{Sn}-0.3\text{Ag}-0.9\text{Zn}$ alloys is main of $\text{Sn}_3\text{O}(\text{OH})_2\text{Cl}_2$.

3.7 Corrosion process analysis

Figure 13 illustrates the corrosion process of the $\text{Sn}-0.3\text{Ag}-0.9\text{Zn}$ alloy in NaCl solution based on the studies above and the PDM theory [28], and the process can be described as follows. A passive film mainly composed of SnO and SnO_2 generates on the surface of the $\text{Sn}-0.3\text{Ag}-0.9\text{Zn}$ alloy when it is immersed in NaCl solution, which is associated with Reaction (c–f). At the same time, the

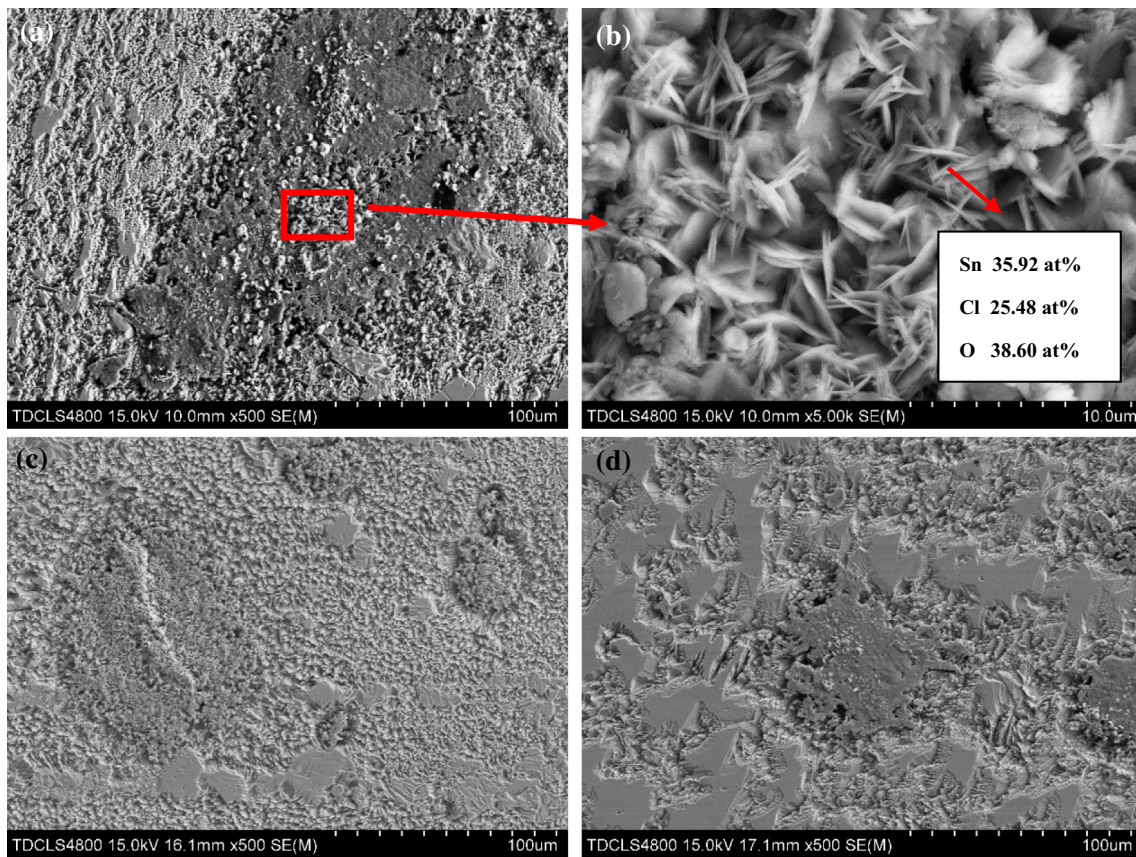


Fig. 12 SEM micrograph on the surface of Sn–0.3Ag–0.9Zn alloy solidified under different cooling rates polarized at $-0.3 V_{SCE}$ for 120 s in 3.5 % NaCl solution at room temperature: **a, b** furnace-cooled, **c** air-cooled, **d** water-cooled

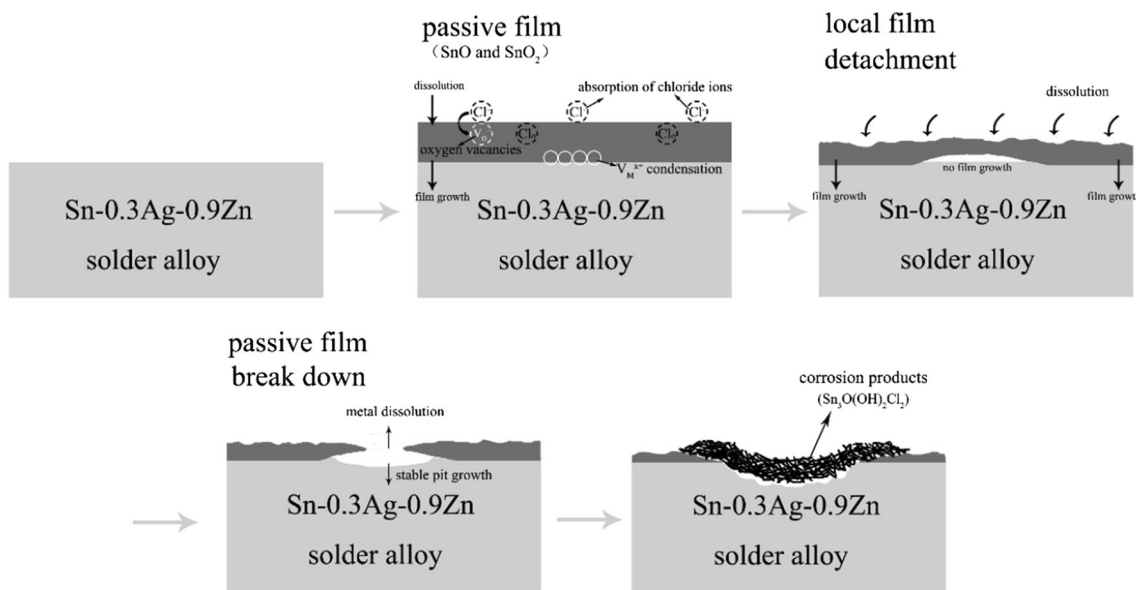


Fig. 13 Schematic diagrams of corrosion process of the Sn–0.3Ag–0.9Zn alloy in NaCl solution

oxygen vacancies ($V_O^{\cdot\cdot}$) in the passive film will absorb and react with the Chloride ions in solution, which will result in that the chloride ion occupied the oxygen vacancy at the

same location, as shown in Reaction (a). Then, based on the Reaction (b), the loss of $V_O^{\cdot\cdot}$ leads to the generation of new cation vacancy (V_M^{x+}), accumulating on the metal/film

interface, which isolates the metal substrate and the passive film and prevents the growth of the passive film. Eventually, the voids formed and the dissolution lead to the nucleation and propagation of pitting and final breakdown of the passive film. With the pit growth and the metal dissolution, the corrosion products ($\text{Sn}_3\text{O}(\text{OH})_2\text{Cl}_2$) generate massily and gather on the corroded surface of the alloy.

4 Conclusions

Based on the present experimental potentiodynamic polarization curves, EIS tests and EN measurements performed with Sn–0.3Ag–0.9Zn alloys samples and the surface observation after the anodic polarization, it concludes that the corrosion resistance of the alloy improves with the increase of the applied cooling rates. The water-cooled alloy without active Zn-rich phase exhibits a microstructure formed by a finer dendrite array associated with smaller AgZn_3 IMCs particles, which reduces the galvanic corrosion between the cathodic IMCs and the anodic Sn matrix. Besides, due to the passivation behavior observed through the electrochemical measurements, the Mott–Schottky and XPS measurements were performed to analyze the semiconductor properties and composition of the passive film formed on the surface of the alloys. It confirms that the stability and protective ability of the passive film formed on water-cooled alloy is higher than that of the furnace-cooled and air-cooled alloy, which is consistent with the results of electrochemical measurements. Furthermore, the corrosion product of the Sn–0.3Ag–0.9Zn alloys is main of $\text{Sn}_3\text{O}(\text{OH})_2\text{Cl}_2$ and the corrosion process exhibits typical local corrosion character.

Acknowledgments The authors are grateful to the China National Funds for Distinguished Young Scientists (Granted No. 51325401), the China National Funds (Granted No. 51131007), the Major State Basic Research Development Program (973 Program) (Granted No. 2014CB046805), the Key Project of Natural Science Foundation of Tianjin (Granted No. 13JCZDJC31900 and 14JCZDJC38700) for grant and financial support.

References

1. M. Abtey, G. Selvaduray, *Mater. Sci. Eng.*, R **27**, 95–141 (2000)
2. D.Z. Li, P.P. Conway, C.Q. Liu, *Corros. Sci.* **50**, 995–1004 (2008)

3. T. Takemoto, T. Funaki, *Mater. Trans.* **43**, 1784–1790 (2002)
4. A. Ahmido, A. Sabbar, H. Zouihri, K. Dakhsi, F. Guedira, M. Serghini-Idrissi, S. El Hajjaji, *Mater. Sci. Eng. B Solid* **176**, 1032–1036 (2011)
5. J.E. Lee, K.S. Kim, M. Inoue, J.X. Jiang, K. Sukanuma, *J. Alloys Compd.* **454**, 310–320 (2008)
6. T.C. Chang, M.H. Hon, M.C. Wang, D.Y. Lin, *J. Electrochem. Soc.* **151**, C484–C491 (2004)
7. Q.V. Bui, N.D. Nam, B.I. Noh, A. Kar, J.G. Kim, S.B. Jung, *Mater. Corros.* **61**, 30–33 (2010)
8. Y.H. Zhang, Y.C. Liu, Y.J. Han, C. Wei, Z.M. Gao, *J. Alloys Compd.* **473**, 442–445 (2009)
9. X. Wang, Y.C. Liu, C. Wei, L.M. Yu, Z.M. Gao, Z.Z. Dong, *Appl. Phys. A Mater.* **96**, 969–973 (2009)
10. W.R. Osório, E.S. Freitas, J.E. Spinelli, A. Garcia, *Corros. Sci.* **80**, 71–81 (2014)
11. M.F.M. Nazeri, A.B. Ismail, A.A. Mohamad, *J. Alloys Compd.* **606**, 278–287 (2014)
12. W.R. Osório, L.R. Garcia, L.C. Peixoto, A. Garcia, *Mater. Design* **32**, 4763–4772 (2011)
13. M.N. Wang, J.Q. Wang, H. Feng, W. Ke, *Corros. Sci.* **63**, 20–28 (2012)
14. W.R. Osório, J.E. Spinelli, C.R.M. Afonso, L.C. Peixoto, A. Garcia, *Electrochim. Acta* **56**, 8891–8899 (2011)
15. J. Hu, T.B. Luo, A.M. Hu, M. Li, D.L. Mao, *J. Electron. Mater.* **40**, 1556–1562 (2011)
16. U.S. Mohanty, K.L. Lin, *Corros. Sci.* **49**, 2815–2831 (2007)
17. U.S. Mohanty, K.L. Lin, *Corros. Sci.* **48**, 662–678 (2006)
18. J. Chen, W. Bogaerts, *Corros. Sci.* **37**, 1839–1842 (1995)
19. D.H. Xia, S.Z. Song, R.K. Zhu, Y. Behnamian, C. Shen, J.H. Wang, J.L. Luo, Y.C. Lu, S. Klimas, *Electrochim. Acta* **111**, 510–525 (2013)
20. L.V. Taveira, M.F. Montemor, M.D. Belo, M.G. Ferreira, L.F.P. Dick, *Corros. Sci.* **52**, 2813–2818 (2010)
21. H.H. Ge, X.M. Xu, L. Zhao, F. Song, J. Shen, G.D. Zhou, *J. Appl. Electrochem.* **41**, 519–525 (2011)
22. X. Wang, Y. Xiu, M.J. Dong, Y.C. Liu, *J. Mater. Sci.: Mater. Electron.* **22**, 592–595 (2011)
23. H. Ohtani, M. Miyashita, K. Ishida, *J. Jpn. Inst. Met.* **63**, 685–694 (1999)
24. T.C. Chang, J.W. Wang, M.C. Wang, M.H. Hon, *J. Alloys Compd.* **422**, 239–243 (2006)
25. M. McCormack, S. Jin, *J. Electron. Mater.* **23**, 715–720 (1994)
26. F. Rosalbino, E. Angelini, G. Zanicchi, R. Carlini, R. Marazza, *Electrochim. Acta* **54**, 7231–7235 (2009)
27. L. Liu, Y. Li, F.H. Wang, *Electrochim. Acta* **54**, 768–780 (2008)
28. D.D. Macdonald, *Pure Appl. Chem.* **71**, 951–978 (1999)
29. M. Wang, J. Wang, H. Feng, W. Ke, *J. Mater. Sci.: Mater. Electron.* **23**, 148–155 (2011)
30. P.E. Alvarez, S.B. Ribotta, M.E. Folquer, C.A. Gervasi, J.R. Vilche, *Corros. Sci.* **44**, 49–65 (2002)
31. U.S. Mohanty, K.L. Lin, *Corros. Sci.* **50**, 2437–2443 (2008)
32. U.S. Mohanty, K.L. Lin, *J. Electron. Mater.* **42**, 628–638 (2013)
33. L.C. Tsao, C.W. Chen, *Corros. Sci.* **63**, 393–398 (2012)